CERN-ACC-NOTE-2020-0024

28 April 2020
michele.carla@cern.ch

Beam-based measurement of the skew-sextupolar component of the radio frequency field of a HL-LHC-type crab-cavity.

M. Carlà, A. Alekou[1], H. Bartosik, L.R. Carver[2]
CERN, CH-1211 Geneva, Switzerland
[1]also at University of Manchester and Cockcroft Institute,
[2]also at University of Liverpool

Keywords: Crab Cavities, HL-LHC, SPS

Summary

Two High Luminosity Large Hadron Collider (LHC) crab-cavity types have been installed in 2018 in the CERN SPS for testing purposes. An attempt to characterize the skew-sextupolar component (a_3) of the radio frequency field of the crab-cavity through beam-based techniques has been carried out. By monitoring with turn-by-turn beam position monitors the betatron motion, it was possible to study the non-linear coupling between the transverse planes resulting from the skew nature of the a_3 component of the crab-cavity. A measurement of the magnitude of a_3 was thus obtained by characterizing amplitude and phase of some of the spectral lines induced by such non-linear coupling. Particular attention was required to disentangle the a_3 contribution of the crab-cavity from the SPS optics non-linearities, that unexpectedly was found to play a dominant role over the faint signal induced by the crab-cavity skew-sextupolar component. A detailed description of the measurement, analysis and the results are here presented.

Contents

1 Introduction

Crab cavities will contribute to an increase in the LHC luminosity output as part of the High-Luminosity LHC upgrade [1, 2, 3, 4]. The transverse radio frequency electric field of the crab cavity is synchronized with the circulating bunches such that the head and tail of the bunches receive an opposite transverse kick while the central part of the bunch stays unperturbed. This condition "tilts" the bunch in the transverse plane and produces a head-on collision. Space constraints, mainly due to the limited separation between the two counter-rotating beams, required the crab cavities to be shaped accordingly, resulting in a non-perfect transverse profile of the dipolar electric field. From simulations presented in [4] and more recently in [5], a sextupolar term has been identified as the main contributor beyond the purely dipolar field with a strength of $\sim$1.5 T/m measured at 10 MV cavity integrated field. Due to the potential beam dynamics implications of such a non-linear field, it was found necessary to verify experimentally the results of the crab-cavity electromagnetic model simulation. The radio-frequency (RF) nature of the crab-cavity field makes it very hard to measure precisely such a non-linear field component in an RF test bench, therefore a beam based measurement was attempted.

During 2018, a prototype of the LHC cavity has been installed in the SPS [6] for test and validation purposes, providing an opportunity to carry out, among other studies the measurement of the aforementioned sextupolar term. The cavities were installed in a vertical kick configuration, turning the quadratic field distortion into a skew-sextupolar field. A skew-sextupole couples in a non-linear manner the vertical and horizontal betatron motion, i.e. when approximated as a thin element the induced kick on to the beam is given by:

$$\begin{cases} \delta p_x = 2a_3 xy \\ \delta p_y = a_3(x^2 - y^2). \end{cases} \tag{1}$$

Since in the SPS the perturbations driven by the vertical betatron motion are not experimentally accessible, for reasons that will be explained in the next section, we concentrate on the study of the vertical plane, where the term x^2 is responsible for the excitation of two modes driven by the horizontal betatron motion only. If the non-linearity strength a_3 is small enough the horizontal beam position x will be dominated by the linear betatron motion. Therefore, at the location of the skew-sextupole the beam position can be approximated as:

$$x(n) \simeq \sqrt{\beta_x^p j_x}\sin(2\pi Q_x n + \psi^p), \tag{2}$$

where n is the turn number, β^p and ψ^p are respectively the betatron amplitude and phase advance at the skew-sextupole, Q_x is the horizontal tune and j_x the horizontal betatron action. Substituting Eq. (2) in Eq. (1) provides:

$$\delta p_y(n) = a_3 x^2(n) = a_3\beta_x^p j_x \sin^2(2\pi Q_x n + \psi^p) = a_3\beta_x^p j_x \frac{1-\cos(4\pi Q_x n + 2\psi^p)}{2}. \tag{3}$$

The previous equation shows that the force induced by the skew-sextupole can be decomposed in two terms: the first one whose amplitude is independent on the turn number and a second one oscillating with frequency $2Q_x$ inducing two vertical modes with frequencies 0 and $2Q_x$ which from now on will be referred as the $V_{0,0}$ and $V_{2,0}$ modes. For simplicity the notation $H_{n,m}$ and $V_{n,m}$ is introduced to indicates respectively horizontal and vertical modes with frequency $nQ_x + mQ_y$, such that $x, y = \mathrm{Re}(H, V_{l,m}e^{2\pi i(lQ_x+mQ_y)n})$.

A simple expression for a mode induced by a generic harmonic driving force is provided in Appendix A. By substituting Eq. (3) in Eq. (27) an explicit expression for the $V_{2,0}$ and $V_{0,0}$ modes is obtained:

$$V_{2,0} = ia_3\frac{j_x\beta_x^p\sqrt{\beta_y^o\beta_y^p}}{4}\left[\frac{e^{i(\psi_y^o-\psi_y^o+2\psi_x^p)}}{1-e^{2\pi i(2Q_x-Q_y)}} + \frac{e^{i(-\psi_y^o+\psi_y^p+2\psi_x^p)}}{1-e^{2\pi i(2Q_x+Q_y)}}\right] \tag{4}$$

$$V_{0,0} = ia_3\frac{j_x\beta_x^p\sqrt{\beta_y^o\beta_y^p}}{2}\cdot\frac{e^{i(\psi_y^o-\psi_y^p)}}{1-e^{-2\pi iQ_y}}, \tag{5}$$

where β_y^o and ψ_y^o are respectively the vertical betatron amplitude and phase advance at the location of observation.

The measurement of the skew-sextupolar component of the crab-cavity is thus carried out by exciting the horizontal betatron motion and measuring by means of turn-by-turn beam position monitors (BPM) [7] the aforementioned characteristic modes: $V_{2,0}$ and $V_{0,0}$.

2 SPS Turn-by-Turn Measurements Optimization

A tune kicker is used to excite the betatron motion in the SPS and by lowering the chromaticity to a value close to 0 it is possible to reduce the decoherence to a level which allows the observation of the coherent beam motion for up to a few hundreds of turns. Ideally, a single low intensity bunch provides the best possible approximation of the single particle dynamics and therefore is the preferred way to carry out turn-by-turn measurements. However this condition is suboptimal in terms of BPM signal quality in the SPS, resulting in a

very noisy read-out. Increasing the bunch intensity is not an option, because of the strong decoherence due to collective effects and beam instabilities observed at low chromaticity. Instead, by employing a train of low intensity bunches, but still with a low chromaticity setting of the machine, it was possible to obtain clear signals with low decoherence in the horizontal plane. Unfortunately the same was not observed in the vertical plane because of the detuning induced by the strong vertical transverse coupling impedance. Figure 1 shows the bunch-by-bunch detuning in the horizontal and vertical planes for a train of 72 bunches. Due to the transverse coupling impedances, the vertical plane is subject to a strong tune-

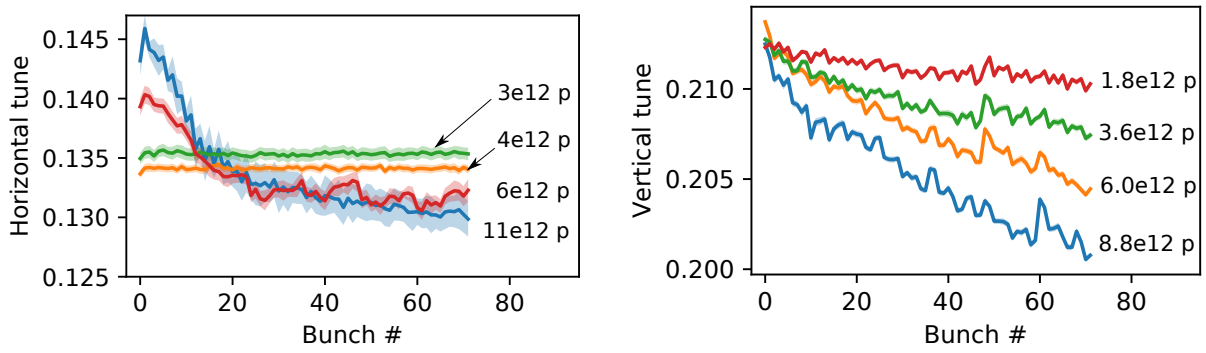

Figure 1: Horizontal (top) and vertical (bottom) bunch by bunch detuning measured in the SPS for trains of 72 bunches of various intensity. The measurement was carried out using a special BPM with bunch-by-bunch capability. In the horizontal plane no detuning is observed until a threshold is reached. This strongly non-linear behavior is the fingerprint of electron-cloud, that requires a certain beam intensity in order for the cloud to build-up. The linear detuning observed in the vertical plane instead can be attributed to transverse impedance.

shift along the train. Since standard SPS BPMs do not have bunch-by-bunch capabilities the overall observed transverse vertical motion of the train of bunches is subject to a fast decoherence due to the strong bunch-to-bunch tune-shift, making it impossible to observe with adequate precision any vertical mode. This is not the case for the horizontal plane, where no major detuning is observed until a threshold of ∼5e12 protons is reached, triggering the build-up of electron-cloud. Therefore by operating below this threshold allows the clear observation of the spectral lines $V_{0,0}$ and $V_{2,0}$. The maximum kick strength to be used to excite the horizontal betatron motion instead was set by the safety margins required to operate the crab-cavity that imposed a maximum trajectory excursion of 10 mm. It was found that the total RF voltage of the SPS accelerating cavity was also playing an important role in the quality of the measurements. Figure 2 shows an example of the measured horizontal beam position for one BPM, repeated for 2 MV and 6 MV total RF voltage. A longer damping time is observed for the higher voltage. To study the behavior, measurements have been systematically repeated in the range from 2 MV to 7 MV. For each RF working point the quality of the turn-by-turn measurement has been evaluated by looking at the BPM-to-BPM spread of the horizontal tune frequency and the average betatron motion damping time as shown in Fig. 3.

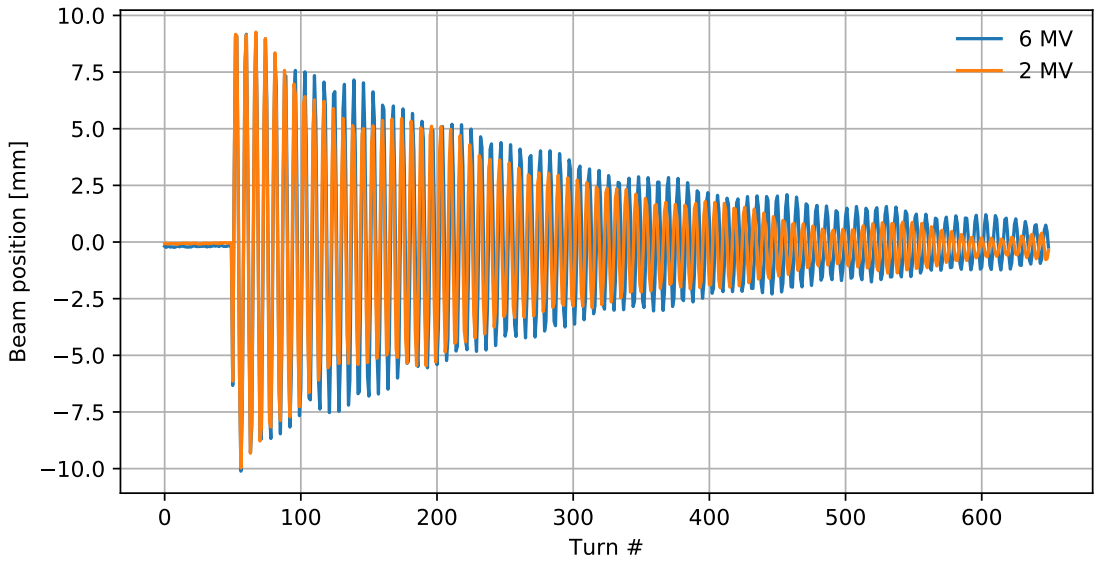

Figure 2: Turn-by-turn horizontal beam position measured with one BPM for two different RF settings: 2 MV and 6 MV total RF voltage.

.

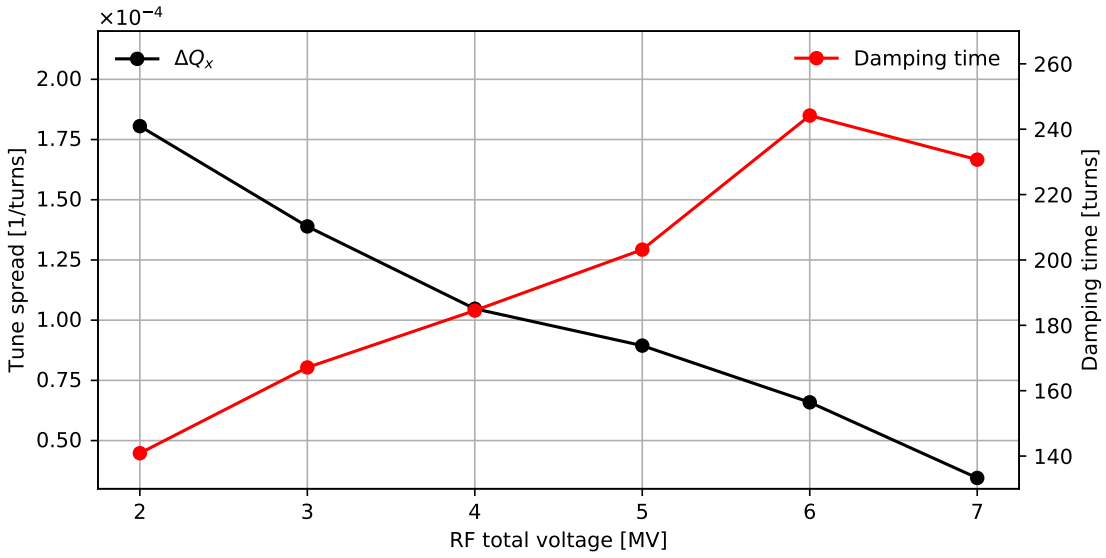

Figure 3: Frequency spread (black) between BPMs and average damping time (red) measured for different RF working point.

A substantial improvement is observed for higher voltages, the larger tune spread for different BPMs and the faster decoherence for lower RF voltage could possibly be caused by uncaptured beam.

3 Turn-by-Turn Signal Analysis

The tune kicker magnet is fired only once for each machine cycle, and consequently only one acquisition is carried out for each cycle. The spectral analysis of the turn-by-turn signal collected by the BPMs is performed independently for each acquisition. The analysis is broken down in three main steps: a first phase of signal preconditioning is followed by the analysis of the linear betatron motion, and finally by the spectral analysis of the modes $V_{0,0}$ and $V_{2,0}$.

To be able to disentangle the contribution to $V_{0,0}$ and $V_{2,0}$ of the skew-sextupolar field under investigation (e.g. the crab-cavity) from any other skew-sextupolar field present in the machine and not correlated to the crab-cavity, the entire procedure is always applied to two experimental datasets: a reference one where the crab-cavity is switched off and a second one where it is on. Once the shift $\Delta V_{2,0}$ and $\Delta V_{0,0}$ of the modes $V_{2,0}$ and $V_{0,0}$ observed between the two datasets has been evaluated, a_3 is determined by matching Eq. (4) and (5) to the measured $\Delta V_{2,0}$ and $\Delta V_{0,0}$ by means of a least square fit. The fit is carried out independently for $\Delta V_{2,0}$ and $\Delta V_{0,0}$, allowing for two independent evaluations of a_3 ($a_3^{V_{2,0}}$ and $a_3^{V_{0,0}}$) and making it possible to cross check the validity of the analysis.

3.1 Signal Preconditioning

Figure 4 shows a typical turn-by-turn signal acquired for 4096 turns with one BPM and the associated spectrum.

While the observed beam betatron oscillation, starting at turn ∼3000 lasts for only a few hundreds turns, a 50 Hz oscillation with constant amplitude is visible throughout the entire acquisition. A similar 50 Hz mode has been observed for many different BPMs but not all of them and with very different amplitude as shown in Fig. 5. Such oscillation is believed to be due to electrical noise that couples directly to the BPM electronics rather than a proper beam motion. Nevertheless it is helpful, for the following analysis to take into account for this 50 Hz noise. The first $\sim$ 3000 turns, before firing the kicker are used to evaluate the phase and amplitude of the 50 Hz mode, allowing to purge the noise from the entire acquired data (Fig. 6). The signal offset is also evaluated from the median of the beam position during the first $\sim$ 3000 turns and removed from the data. This initial data cleanup (removal of the offset and 50 Hz line) is repeated independently BPM by BPM.

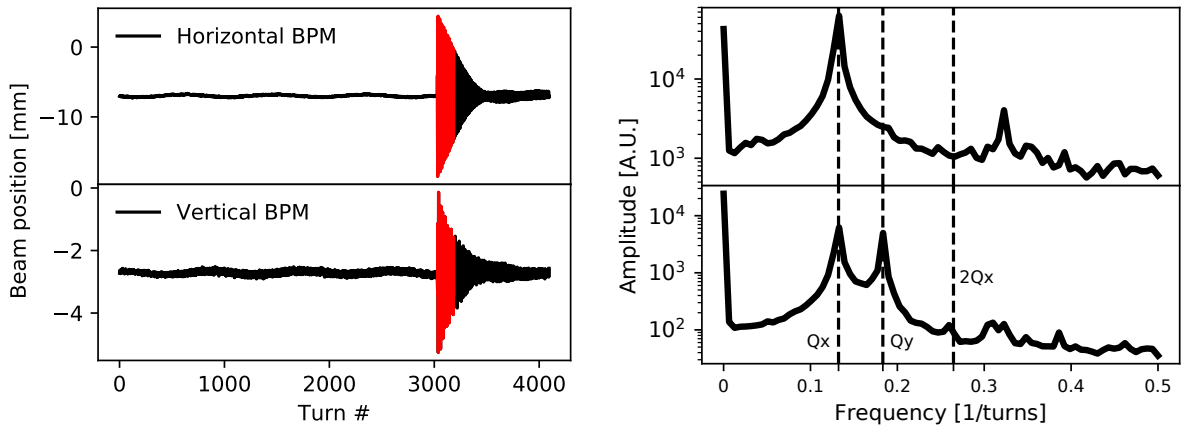

Figure 4: Typical turn-by-turn beam position measurement for the horizontal and vertical plane (left). The kicker magnet is fired only after ∼3000 turns allowing to sample the background noise and beam position offset, while the spectral analysis is carried out on the portion shown in red only. The Fourier spectrum (right) of the turn-by-turn beam position (red portion only) shows clearly the peaks relative to the horizontal and vertical tune, while the $V_{2,0}$ barely appears over the noise floor and $V_{0,0}$ requires some major analysis in order to distinguish it from the beam position offset.

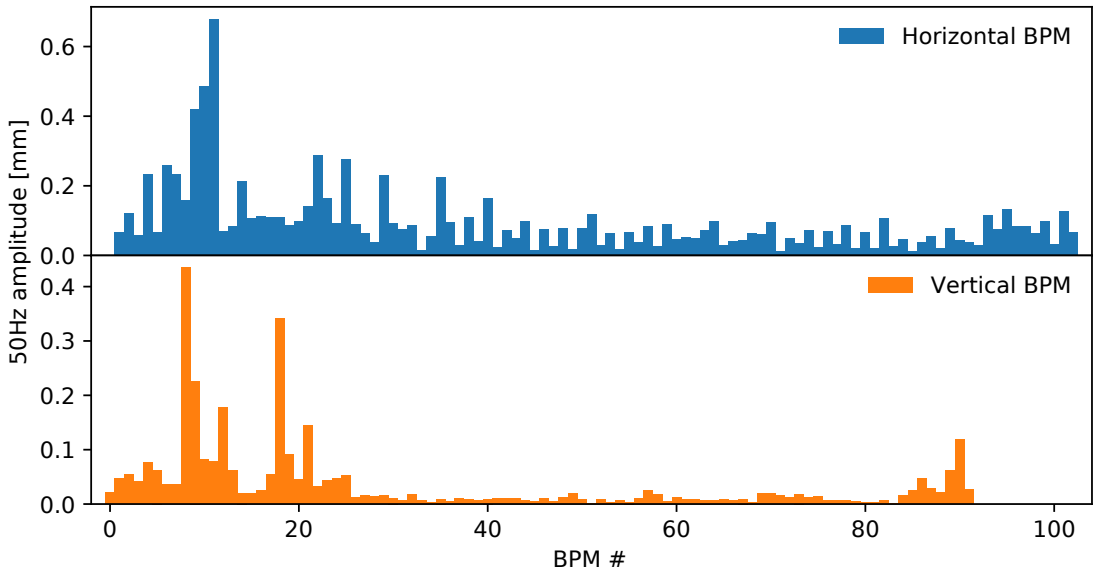

Figure 5: Amplitude of the 50 Hz noise measured by each BPM sampled for ∼3000 turns.

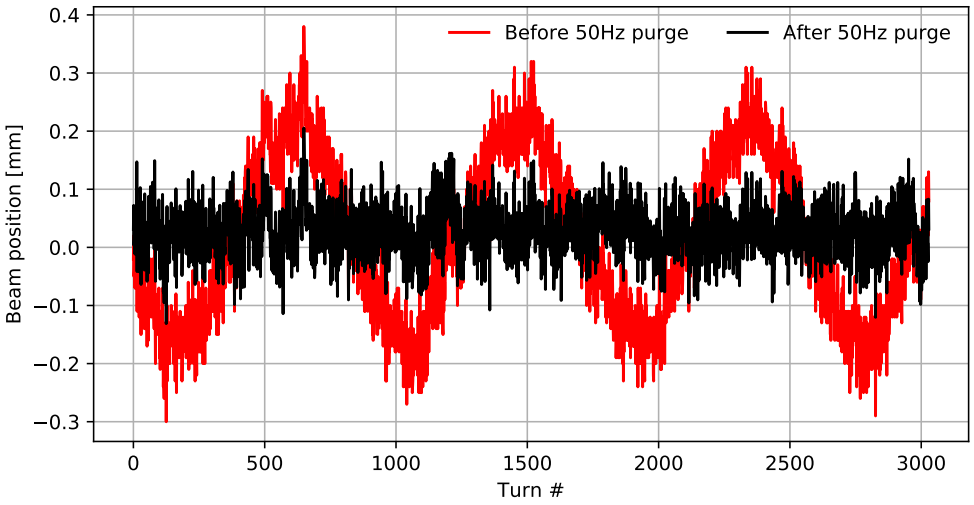

Figure 6: The 50 Hz noise appears clearly (red) in the beam position measured during the first 3000 turns by one of the horizontal BPM. In black the same signal after the 50 Hz "purging" process.

3.2 Analysis of the Linear Betatron Motion

The analysis of the linear betatron motion aims to estimate precisely a few parameters such as the horizontal tune, action and damping time required to carry out the following analysis of the modes $V_{2,0}$ and $V_{0,0}$. The analysis is broken down into several steps:

1. The frequency (Q_x) of the horizontal tune (the mode $H_{1,0}$) is established from the signal collected by the horizontal BPMs. This is achieved by carrying out a spectral analysis "à la Laskar" [8, 9, 10] independently BPM by BPM.

2. Since Q_x is supposed to be independent from the observation point (BPM) a more accurate estimate of Q_x is obtained by calculating the median of Q_x measured by each horizontal BPM.

3. A first guess for the real and imaginary part of $H_{1,0}$ is evaluated individually for each BPM as:
$$H_{1,0} = \frac{1}{N}\sum_{n=0}^{N} x(n)e^{2\pi i Q_x n}w(n), \tag{6}$$
where $w(n)$ is the Hanning window function.

4. The estimate of the mode $H_{1,0}$ previously obtained is used as the initial condition for a least squares fit, where the damping time τ_x and the amplitude $|H_{1,0}|$ are optimized to minimize the expression:
$$[x(n) - \mathrm{Re}(H_{1,0}e^{2\pi i Q_x n}e^{-n/\tau_x})]^2. \tag{7}$$

Here a simple exponential decay is introduced to represent the signal damping, while a more complicated law would be required to describe properly the decoherence process. On the other hand the low chromaticity and the small number of turns used to carry out the measurement makes the approximation acceptable and keeps the fit simple.

5. Since the damping τ_x is also independent from the observation point (BPM) a more accurate estimate of the damping time is obtained as the median of τ_x measured by each horizontal BPM.

6. The damping is removed from the signal collected by each horizontal BPM by normalizing the data with an exponential damping law with damping rate τ_x.

7. Real and imaginary parts of $H_{1,0}$ are evaluated again, this time using the un-damped signal obtained in the previous step by using Eq. (6).

8. Finally the horizontal betatron action j_x is evaluated by fitting the amplitude of $H_{1,0}$ at each BPM with a model of the SPS optics.

3.3 Spectral Analysis of the Modes $V_{0,0}$ and $V_{2,0}$

Once Q_x, τ_x and j_x have been evaluated it is possible to proceed with the analysis of the modes $V_{0,0}$ and $V_{2,0}$. Also in this case the procedure involves several steps:

1. The turn-by-turn data $y(n)$ collected by the vertical BPMs is renormalized by an exponential damping law with damping rate $\tau_x/2$. In fact while the horizontal linear betatron motion ($H_{1,0}$) decoheres with a characteristic time τ_x, the mode $V_{2,0}$ decoheres two times faster, having two times higher frequency [11, 12].

2. Real and imaginary part of $V_{2,0}$ are evaluated as:

$$V_{2,0} = \frac{1}{N}\sum_{n=0}^{N} y(n)e^{2\pi i 2Q_x n}w(n). \tag{8}$$

3. $V_{0,0}$ describes a mode with frequency 0 that is a closed orbit distortion. Since many other contributions to the beam orbit are to be expected (e.g. magnets misalignment, BPMs misalignment), a slightly different approach is used to evaluate the mode $V_{0,0}$. Since the closed orbit distortion $V_{0,0}$ is present only when the horizontal betatron motion is excited, it is possible to evaluate $V_{0,0}$ from the orbit change observed before and after firing the kicker. The orbit in presence of the horizontal betatron motion is computed by averaging $y(n)$ over N turns after firing the kicker while the N turns before are used to compute the still beam reference orbit. A bigger number of turns to compute the reference orbit could be potentially used but would not improve significantly the analysis while increasing the risk of spoiling it because of slow uncontrolled orbit drift or other systematic effects.

Every step of the spectral analysis has been carried out using the first $N = 128$ turns after firing the kicker, this number has been initially chosen for convenience and because it matches roughly the damping time of the modes $V_{0,0}$ and $V_{2,0}$. Further tests have shown that no particular improvement was obtained by increasing N, therefore it was left at 128.

4 MAD-X/PTC Tracking Test

A first test of the analysis procedure was carried out on simulated data. The software MAD-X/PTC was used to track the turn-by-turn orbit of a single particle at every BPM in the SPS. The simulation was setup to reproduce as close as possible the experimental conditions to be used for the crab-cavity measurements, the Q26 optics was used and a single horizontal kick at the same location of the SPS tune kicker was used to excite the horizontal betatron motion. The kick strength was set such as to produce an horizontal betatron amplitude of $\sim$8 mm ($j_x \simeq 2.2 \times 10^{-7}$ m). Two simulations are carried out, the first one (reference) using the bare lattice, while the second one includes a skew-sextupole located at the same position where the crab-cavity prototypes have been installed. The skew-sextupole is simulated as a static thin lens with integrated field a_3: 10^{-2} m^{-2} (MAD-X unit for integrated thin lens multipole strength). The two simulations are analyzed following the procedure described in the previous section and the shift $\Delta V_{2,0}$ and $\Delta V_{0,0}$ observed between the two simulations is used to establish a_3. Figure 7 shows the result of the analysis. The discrepancy between

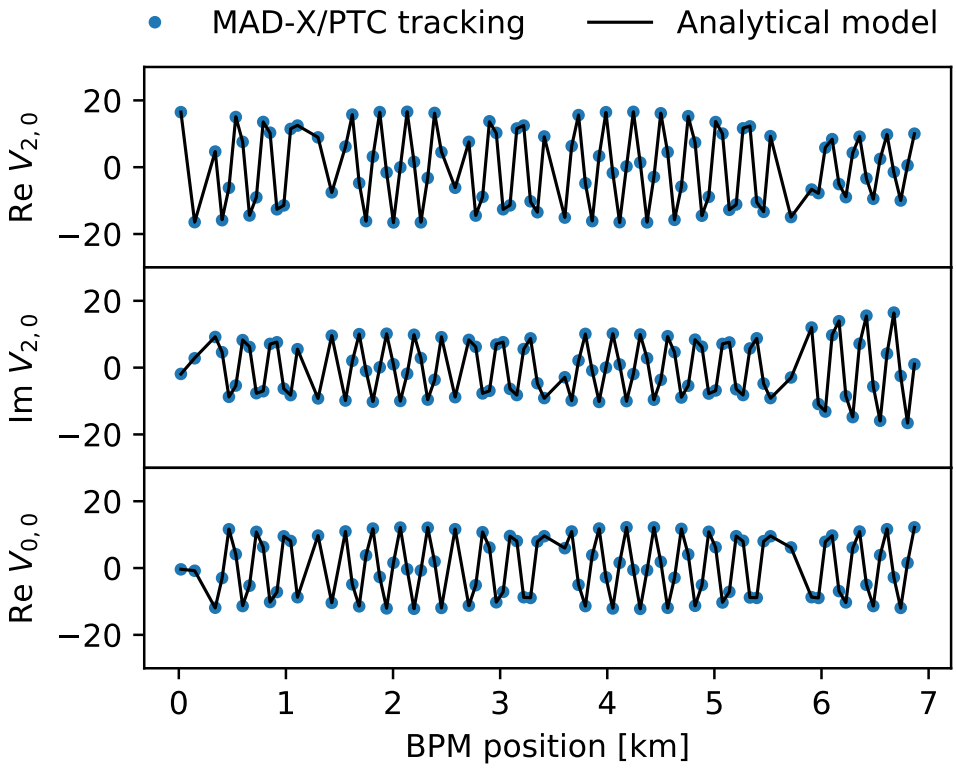

Figure 7: Results of the spectral analysis of the turn-by-turn data simulated with MAD-X/PTC (blue). A fit of the analytical model of $V_{2,0}$ and $V_{0,0}$ is also shown (black). The values of a_3 obtained from the two independent fit of $V_{2,0}$ and $V_{0,0}$ is $a_3^{V_{2,0}} = 9.94 \times 10^{-3}$ 1/m^2 and $a_3^{V_{0,0}} = 9.95 \times 10^{-3}$ 1/m^2, close to the skew-sextupole strength used in the MAD-X/PTC simulation of 1×10^{-2} 1/m^2.

the skew-sextupolar field strength a_3 retrieved from the spectral analysis and the value set

in the MAD-X/PTC simulation is $\sim 0.5\%$, well below the experimental uncertainties that dominate the measurements as will be shown in the next sections.

5 Static Skew-Sextupole Measurements

In order to prove the experimental setup, a measurement was performed on the 20$^{\text{th}}$ October 2017 at the SPS by using a static skew-sextupolar field. The Q20 optics was used and the chromaticity knobs were set to QPH: 0 and QPV: -0.45. The injector was configured to provide single batches of 72 bunches at each cycle with a total intensity of $\sim 2.8 \times 10^{12}$ p. The kicker voltage was set to 10 kV resulting in a horizontal betatron action $j_x \simeq 2.2 \times 10^{-7}$ m and the total RF voltage was set to 4.5 MV.

Since no skew-sextupole magnets are installed in the SPS, the feed-down resulting from a vertical orbit bump in an octupole was used instead to produce a skew-sextupolar field with strength:

$$a_3 = y^p b_4, \tag{9}$$

where y^p is the vertical beam orbit at the octupole location and b_4 is the octupole integrated field. For this purpose the octupole LOE33002 was selected, as the horizontal dispersion (η_x =1.1 m) at this location is the lowest possible among all the individually powered extraction octupoles. Several data-sets have been acquired for a vertical orbit bump of ± 5 mm (Fig. 8) and an integrated octupolar field of b_4=0 m^{-3}, ± 2 m^{-3} and ± 5 m^{-3}, each dataset consisting of a few tens of cycle acquisitions. Once again the analysis described previously

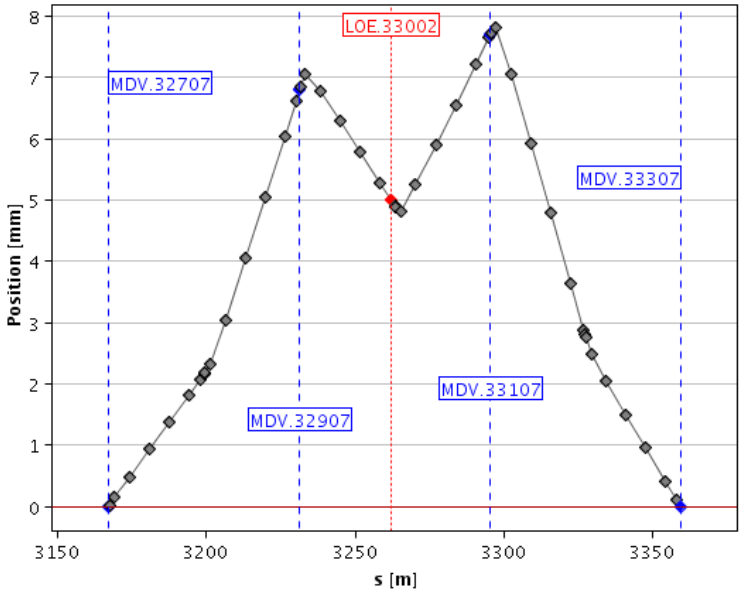

Figure 8: Four vertical orbit correctors (MDV32707, MDV32907, MDV33107 and MDV33307) haven been used to bump the beam at the octupole location (LOE33002) and produce a skew-sextupolar field by feed-down effect.

is carried out, and the shift $\Delta V_{2,0}$ and $\Delta V_{0,0}$ observed between the data-set acquired with b_4=0 m^{-3} and each other dataset is used to establish independently a_3. Figure 9 shows the

result of the fitting procedure for one of the configuration used in the measurement with a positive bump of 5 mm and b_4=−5 m^{-3} a similar result is obtained for the other cases. The result of the fit for every configuration under test is shown in Table 1. The errors on

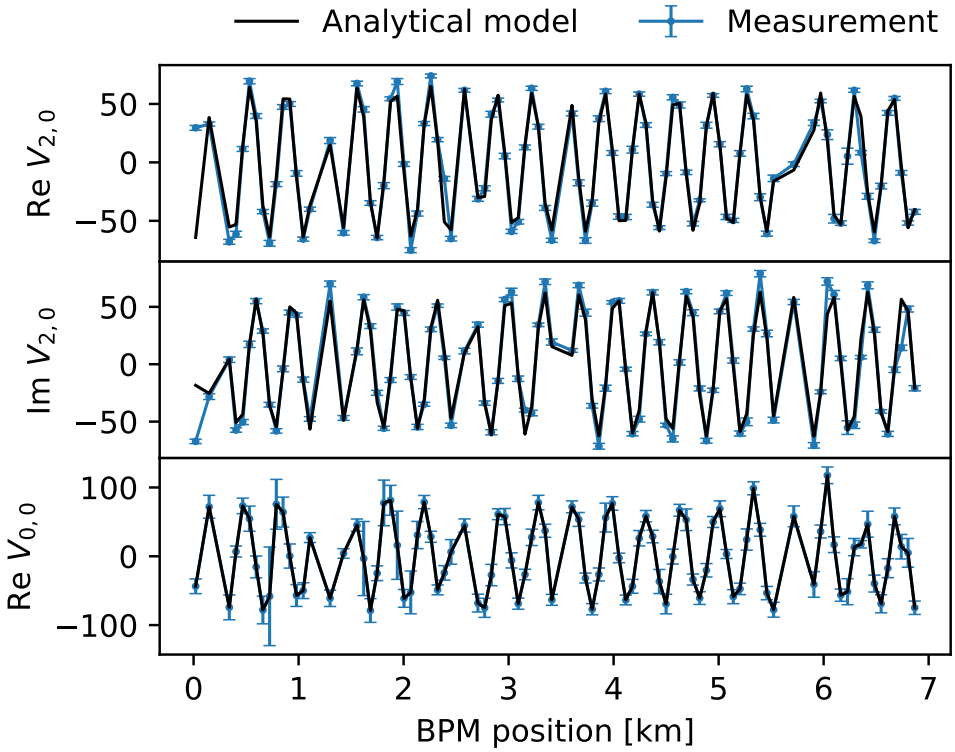

Figure 9: Variation (blue) of the real and imaginary part of the $V_{2,0}$ spectral line and the $V_{0,0}$ orbit distortion induced by switching on the static sextupolar field. The error bars represent the measurement-to-measurement statistic fluctuations. The analytical model (black) is fitted to the data to obtain the skew-sextupole strength.

$a_3^{V_{2,0}}$ and $a_3^{V_{0,0}}$ represent the standard error derived from the covariance matrix of the least square fit. The systematic deviation of $a_3^{V_{2,0}}$ and $a_3^{V_{0,0}}$ with respect to the expected a_3 could be attributed to many issues such as:

- Beta-beating at the octupole location.
- Errors in the octupole current-to-field calibration curve.
- Error in the bump amplitude due to beta-beating.
- Error in the bump amplitude due to error in the orbit correctors current-to-field calibration curve.

The same explanation does not hold for the value of $a_3^{V_{0,0}}$, which is systematically higher compared to $a_3^{V_{2,0}}$. On the other hand the worst discrepancy of $a_3^{V_{0,0}}$ with respect to the expected a_3 is found to be ∼42% and ∼27% in the case of $a_3^{V_{2,0}}$, values considered still

Table 1: Value of the skew-sextupolar integrated field obtained in every single configuration under test. The expected value of a_3 is derived from the amplitude of the orbit bump in the octupole and the octupole strength (b_4). The number of acquired cycles for the octupole on/octupole off datasets is also shown.

Acquired cycles	Bump [mm]	b_4 [m^{-3}]	Expected a_3 [m^{-2}]	$a_3^{V_{2,0}}$ [m^{-2}]	$a_3^{V_{0,0}}$ [m^{-2}]
30 / 15	5	5	$2.5 \cdot 10^{-2}$	$1.827 \cdot 10^{-2} \pm 4.6 \cdot 10^{-4}$	$2.357 \cdot 10^{-2} \pm 1.3 \cdot 10^{-3}$
30 / 86	5	2	$1.0 \cdot 10^{-2}$	$8.999 \cdot 10^{-3} \pm 1.9 \cdot 10^{-4}$	$1.177 \cdot 10^{-2} \pm 5.9 \cdot 10^{-4}$
31 / 28	-5	2	$-1.0 \cdot 10^{-2}$	$-9.699 \cdot 10^{-3} \pm 1.9 \cdot 10^{-4}$	$-1.377 \cdot 10^{-2} \pm 5.3 \cdot 10^{-4}$
31 / 32	-5	5	$-2.5 \cdot 10^{-2}$	$-2.237 \cdot 10^{-2} \pm 4.8 \cdot 10^{-4}$	$-2.657 \cdot 10^{-2} \pm 9.2 \cdot 10^{-4}$
31 / 20	-5	-5	$2.5 \cdot 10^{-2}$	$2.364 \cdot 10^{-2} \pm 4.7 \cdot 10^{-4}$	$2.991 \cdot 10^{-2} \pm 8.5 \cdot 10^{-4}$
31 / 22	-5	-2	$1.0 \cdot 10^{-2}$	$1.056 \cdot 10^{-2} \pm 2.1 \cdot 10^{-4}$	$1.221 \cdot 10^{-2} \pm 5.5 \cdot 10^{-4}$
28 / 17	5	-2	$-1.0 \cdot 10^{-2}$	$-7.513 \cdot 10^{-3} \pm 1.5 \cdot 10^{-4}$	$-1.058 \cdot 10^{-2} \pm 7.7 \cdot 10^{-4}$
28 / 16	5	-5	$-2.5 \cdot 10^{-2}$	$-2.035 \cdot 10^{-2} \pm 3.6 \cdot 10^{-4}$	$-2.448 \cdot 10^{-2} \pm 8.3 \cdot 10^{-4}$

adequate for the purpose of the measurement. Since the observed systematic deviations are by far dominant compared to the measurement-to-measurement fluctuations, the number of acquired cycles for each data set can be decreased considerably without compromising the results. This aspect plays an important role in the context of the crab-cavity testing activities where the assigned time for this measurement is limited.

6 Crab-cavity Measurements

A short time span was assigned for crab cavity tests in October 2018 during which the a_3 measurement was carried out. The time limitation constrained the attempts to a minimum and forced to keep the setup as simple as possible. Unlike the case of a static skew-sextupole the crab-cavity produces a time dependent field dominated by a strong dipolar vertical kick with a weak skew-sextupolar component on top of it. To maximize the effect induced by the crab-cavity on the beam the cavity was always operated on crest: the passage of the beam was synchronized with the maximum field in the cavity. During the test only one of the two installed crab-cavities was operational, limiting the total crab-cavity voltage to $\sim$1 MV. Three data sets were acquired, two with the maximum allowed crab cavity voltage but opposite phase ($\pm$1 MV) and one with the cavity set to the minimum voltage of 100 kV: the crab-cavity RF system in fact did not allow operating with a lower cavity voltage.

To provide a relative measurement of the field distortion independent of the crab-cavity voltage the measurement of the skew-sextupolar component a_3 is renormalized by the cavity integrated field. Therefore it is important to be able to asses correctly the operating field of the cavity for each one of the different acquired datasets. Instead of relying on the radio frequency measurement, the crab-cavity voltage is determined by measuring the beam vertical closed orbit distortion induced by the dipolar component of the field. More importantly this approach allows to take out any effect due to the time dependent nature of the crab-cavity field and the non flat frequency response of the BPMs [13], that otherwise would result in a non trivial relation between the measured and effective beam position. In fact those effects

affect in the same way both, the measurement of closed orbit and of the modes $V_{0,0}$ and $V_{2,0}$ from which a_3 is deduced. The orbit estimation is carried out for each vertical BPM by calculating the median of the beam position during the first ∼3000 turns before firing the kicker. The crab-cavity integrated field is inferred from the measured vertical orbit by fitting the following model for the closed orbit distortion Δy produced by a thin dipole:

$$\Delta y = \sqrt{\beta_y^o \beta_y^p} \frac{\cos(\pi Q_y/2 - |\psi_y^o - \psi_y^p|)}{2\sin(\pi Q_y/2)}. \tag{10}$$

Figure 10 shows the result of the closed orbit fitting procedure for the measurement obtained when shifting the crab-cavity voltage from 100 kV to −1 MV, a similar result is observed when shifting the cavity voltage from 100 kV to 1 MV. The observed integrated cavity field obtained with this method (−0.62 MV) appears to be sensibly smaller compared to what is expected, the discrepancy is to be attributed to the limited precision of the RF measurements and to the non-trivial behavior of the BPMs in presence of a time dependent beam position structure as the one produced by the crab-cavity field. Figure 11 shows the measured $\Delta V_{2,0}$

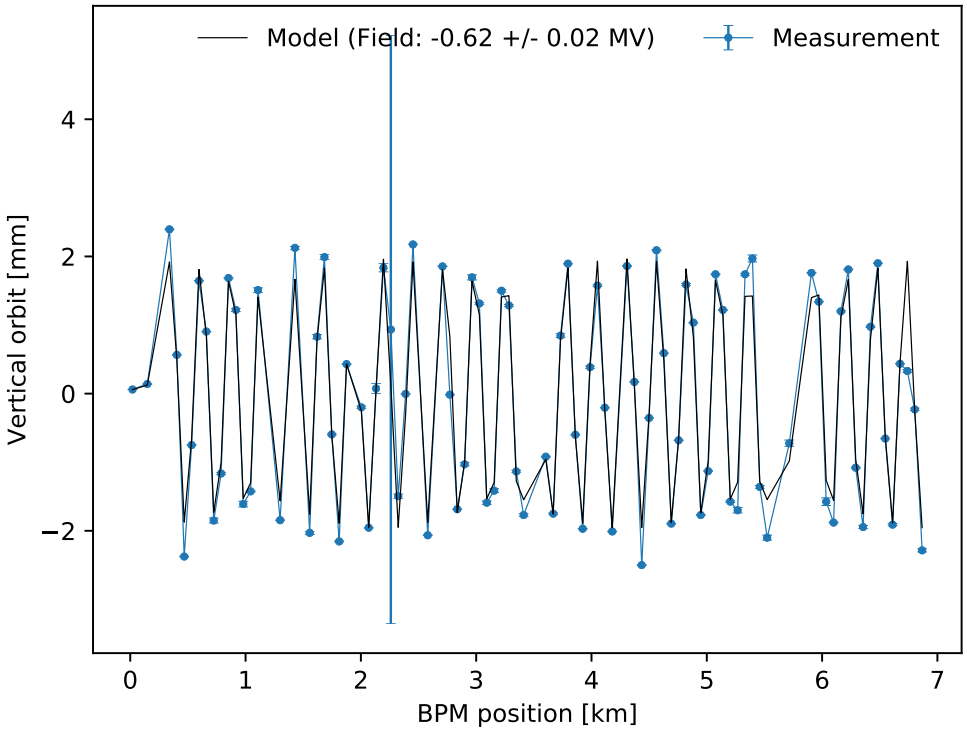

Figure 10: Measured vertical closed orbit shift observed when shifting the cavity voltage from 100 KV to 1 MV (blue), the error bars represent the statistical measurement to measurement fluctuations calculated as one standard deviation divided by the square root of the number of measurements. An analytical closed orbit model (black) is fitted to establish the crab-cavity integrated field.

and $\Delta V_{0,0}$ observed when switching the crab cavity field from 100 kV to ∼1 MV. For the $V_{0,0}$ mode there is only minor agreement between the analytical model and measurements, but

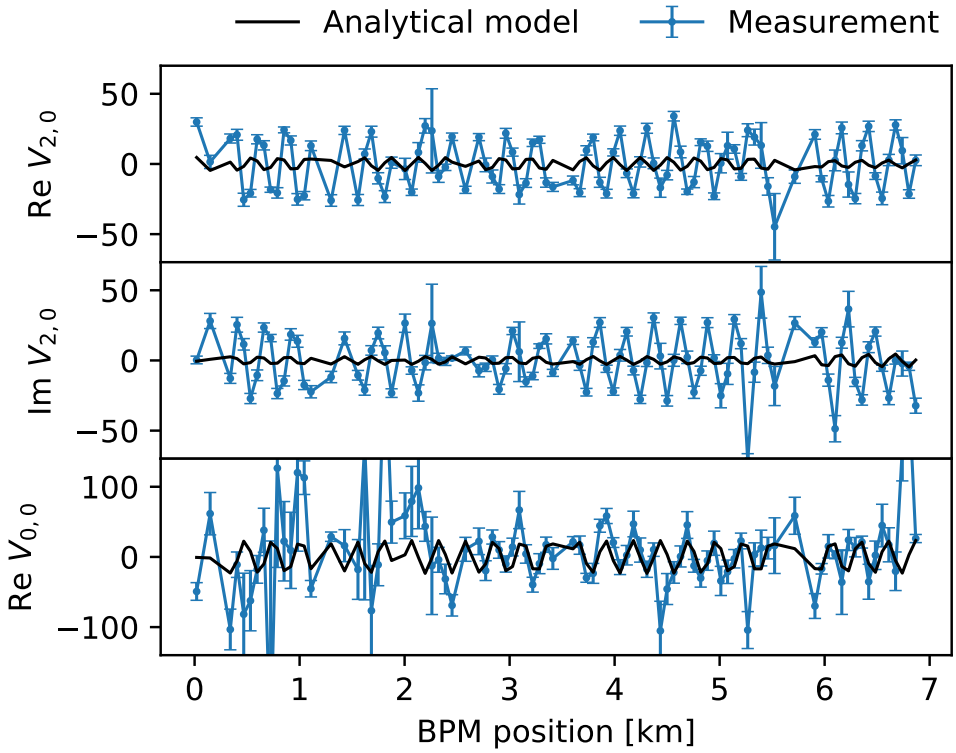

Figure 11: Variation (blue) of the real and imaginary part of the $V_{2,0}$ and $V_{0,0}$ modes induced by switching on the crab-cavity field from 100 kV to ∼1 MV. The error bars represent the measurement-to-measurement statistic fluctuations. The analytical model (black) is fitted to the data to obtain the skew-sextupole strength. The discrepancy in the case of the mode $V_{2,0}$ is striking while a certain agreement can be seen for $V_{0,0}$.

for the $V_{2,0}$ mode the discrepancy is even worse. A similarly disappointing result is obtained when switching the crab cavity field from 100 kV to ∼−1 MV. To shed some light on the issue, the fit of $\Delta V_{2,0}$ is repeated but considering a_3 as a complex parameter, where the magnitude $|a_3|$ represents the strength of the skew-sextupolar field and the phase $\Delta\psi$ allows to take into account for example for a possible error in the crab-cavity phase advance. As shown in Fig. 12 the added degree of freedom allows for a much better agreement between the analytical model and experimental data. The results of the fit for the two crab-cavity field configurations (±1 MV) have been collected in Table 2. The magnitude of a_3 is shown both in $1/(\mathrm{m}^2{\cdot}\mathrm{MV})$, MAD-X units normalized by the crab-cavity voltage and in $\mathrm{T}/(\mathrm{m}{\cdot}\mathrm{MV})$, following the same definition as in [4] [1]. The non zero $\Delta\psi$ could be explained by a strong distortion of the linear optics, possibly due to the large vertical closed orbit induced by the crab-cavity. To exclude this possibility the measured horizontal phase advance (the phase of the mode $H_{1,0}$) has been compared to the one expected from the SPS optics model. Figure 13 shows the horizontal phase-beating measured by every horizontal BPM derived from the 3 data-sets (±1MV and 0.1MV), for completeness also the phase-beating obtained from one

[1]Switching from $\mathrm{T}/(\mathrm{m}{\cdot}\mathrm{MV})$ to $1/(\mathrm{m}^2{\cdot}\mathrm{MV})$ requires to divide by the beam rigidity and multiply by 2 to take into account for the factorial term introduced by the different definition of the field gradient.

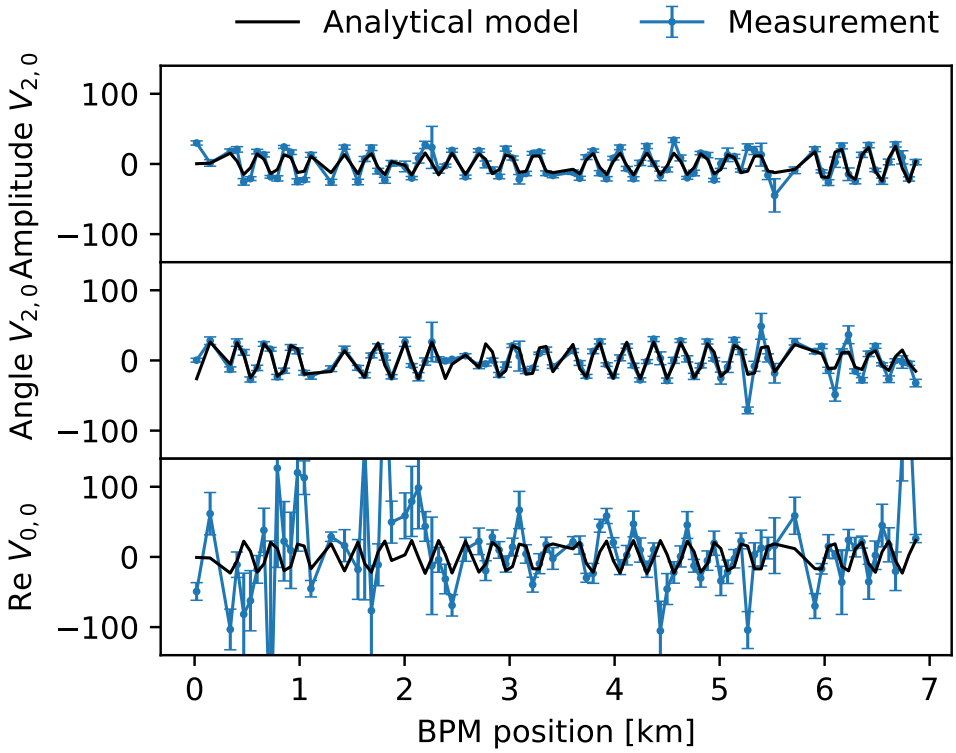

Figure 12: Variation (blue) of the real and imaginary part of the $V_{2,0}$ and $V_{0,0}$ modes induced by switching on the crab-cavity field from 100 kV to ∼1 MV. Compared to to Fig. 11 a phase parameter is introduced in the fit of $V_{2,0}$, providing a much better agreement.

of the dataset acquired during the static skew-sextupole test is shown.

The phase error appears to be dominated by an overall offset that change from data-set to data-set, the effect is more pronounced in the case of the static skew-sextupole test. Such phase offset is not compatible with the beating footprint typical of an optics error. Instead is likely to be attributed to the addidtional decoherence introduced by the octupole used to induce the skew-sextupolar field. In fact the change in decoherence can affect the spectral analysis, resulting in a systematic error of the estimated phase. Unfortunately the vertical phase-beating was not measured since the vertical betatron motion was not excited during the measurements, therefore a direct estimation of any optics distortion affecting the vertical plane is not possible. It is still possible to establish the effect in the vertical plane in a worst case scenario, where an error is located at a position of maximum vertical beam cross section with $\beta_y \simeq 103$ m that in the SPS corresponds also to a horizontal waist with $\beta_x \simeq 21$ m. In this case a vertical phase-beating about 5 times bigger compared to what was observed in the horizontal plane is expected, a value still too small to explain the observed mismatch of the phase of the mode $V_{2,0}$. Explaining the wrong value of the measured V_{20} phase requires a mechanism, tied to the presence of voltage in the crab-cavity and able to excite a vertical betatron mode with frequency $2 \cdot Qx$. In fact, any contribution to the modes V_{20} and V_{00} not dependant on the crab-cavity field would affect equally every data-set having no effect on the differences $\Delta V_{2,0}$ and $\Delta V_{0,0}$ thus not affecting the estimate of $a_3^{V_{2,0}}$ and $a_3^{V_{0,0}}$. The only not

Table 2: Value of the skew-sextupolar integrated field obtained in every single configuration under test. ψ represents the phase of the complex parameter $a_3^{V_{2,0}}$. The set crab-cavity field and the measured field change between the two used data-sets is also shown together with the number of acquired cycles for the crab-cavity field configurations 100 kV / ±1 MV.

Cycles #	Set field [MV]	Δfield [MV]	ψ [deg]	$\lvert a_3^{V_{2,0}} \rvert$ [1/(m^2·MV)] [T/(m·MV)]	$a_3^{V_{0,0}}$ [1/(m^2·MV)] [T/(m·MV)]
10 / 6	0.1 / 1	0.762	-82.4±2.5	$2.046 \cdot 10^{-2} \pm 8.6 \cdot 10^{-4}$	$2.512 \cdot 10^{-2} \pm 4.0 \cdot 10^{-3}$
				$0.887 \pm 3.7 \cdot 10^{-2}$	$1.089 \pm 1.8 \cdot 10^{-1}$
10 / 4	0.1 / -1	-0.621	-84.2±2.2	$2.492 \cdot 10^{-2} \pm 9.9 \cdot 10^{-4}$	$-2.039 \cdot 10^{-2} \pm 5.5 \cdot 10^{-3}$
				$1.080 \pm 4.3 \cdot 10^{-2}$	$-0.884 \pm 2.4 \cdot 10^{-3}$

disappearing contributions are the ones driven by the crab-cavity field, being the crab-cavity field the only machine parameter changed during the entire measurement process.

7 Other Contributions to the Modes $a_3^{V_{2,0}}$ and $a_3^{V_{0,0}}$

Two mechanisms connected to the vertical orbit that affect the modes $V_{2,0}$ and $V_{0,0}$ have been identified:

1. Feed-down effect from octupoles.
2. Second order contribution due to normal sextupoles.

As will be discussed in the following both effects play an important role in the analysis.

7.1 Octupoles Induced Feed-Down

While no octupole was purposely switched on during the measurements, it is known that a certain amount of octupolar field is always present in the SPS [14], likely due to the octupoles remanent field that persists even when the magnets power supply is switched off or as field error in other elements. To evaluate the feed-down contribution of a single thin octupole, the vertical beam orbit y^p at the octupole location is calculated by means of Eq. (10) and plugged into Eq. (9) to obtain the resulting skew-sextupolar field strength. After that Eqs. (4) and (5) are used as usual to obtain the contribution to modes $V_{2,0}$ and $V_{0,0}$. The process is iterated over every single octupole in the SPS optics and each individual contribution added together.

7.2 Normal Sextupoles Second Order Effects

The contribution to the modes $V_{2,0}$ and $V_{0,0}$ from normal sextupoles instead is a "two step process". The vertical orbit induced by the crab-cavity is responsible for a skew-quadrupolar field such that:

$$\begin{cases} \delta p_x = y^p b_3 \cdot y \\ \delta p_y = y^p b_3 \cdot x. \end{cases} \tag{11}$$

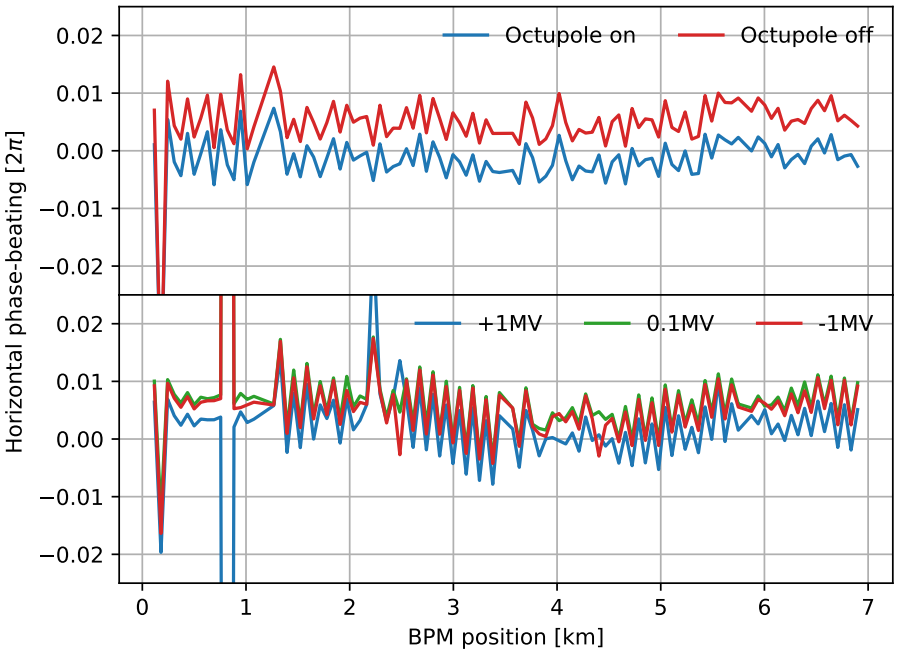

Figure 13: Difference between measured horizontal phase-advance with respect to the ideal value from the optics model. The plots have been realized using the three data-sets collected during the crab-cavity measurements (bottom) and two of the data-sets collected for the static skew-sextupole (top) relative to the same bump configuration and with octupole strength b_4: $0\,\mathrm{m}^{-3}$ and $5\,\mathrm{m}^{-3}$, while every other configuration provided similar results.

Where b_3 is the integrated field of the normal sextupole. By following the same procedure introduced in chapter 1, the driving force at a generic sextupole s is calculated by substituting Eq. (2) in Eq. (11), providing:

$$\delta p_y(n) = y^s b_3^s \cdot x(n) = y^s b_3^s \sqrt{\beta_x^s j_x} \cdot \sin(2\pi Q_x n + \psi^s), \tag{12}$$

from which the mode $V_{1,0}^s$ induced by the sextupole s is calculated by using Eq. (25):

$$V_{1,0}^s = b_3^s \sqrt{2 j_x \beta_x^s \beta_y^s \beta_y^o} \left[\frac{e^{i(\psi_x^s + \psi_y^o - \psi_y^s + 2\pi(Q_x - Q_y))}}{1 - e^{2\pi i (Q_x - Q_y)}} - \frac{e^{i(\psi_x^s - \psi_y^o + \psi_y^s + 2\pi(Q_x + Q_y))}}{1 - e^{2\pi i (Q_x + Q_y)}} \right]. \tag{13}$$

The overall $V_{1,0}$ is obtained by adding together the contribution of each individual normal sextupole. Because of the large number and strength of the sextupoles the amplitude of the mode $V_{1,0}$ is substantial and therefore can drive non negligible second order effect. In particular when the modes $V_{1,0}$ and $H_{1,0}$ get *mixed* together by the non-linear coupling introduced by the normal sextupoles, the modes $V_{2,0}$ and $V_{0,0}$ are excited. The kick induced on the beam by a normal sextupole is:

$$\begin{cases} \delta p_x = b_3 \cdot (x^2 - y^2) \\ \delta p_y = 2 b_3 \cdot xy. \end{cases} \tag{14}$$

By substituting $x(n) = \mathrm{Re}(H_{1,0} \cdot e^{2\pi i Q_x n})$ and $y(n) = \mathrm{Re}(V_{1,0} \cdot e^{2\pi i Q_x n})$ in the previous expression we obtain for $\delta p_y(n)$:

$$\delta p_y = 2b_3 \cos(2\pi Q_x n + \psi^s) \cdot \cos(2\pi Q_x n)\, \mathrm{Re}(H_{1,0}) \sum_s V^s_{1,0}. \tag{15}$$

As in the case of Eq. (3), this expression can be decomposed as the sum of two terms: the first one whose amplitude is independent on the turn number and a second one oscillating with frequency $2 \cdot Q_x$ and therefore exciting the two modes $V_{2,0}$ and $V_{0,0}$. By plugging Eq. (15) in Eq. (25) we finally obtain the second order contribution to the modes $V_{2,0}$ and $V_{0,0}$ induced by the normal sextupole z:

$$V_{2,0} = b_3 \frac{j_x \sqrt{\beta^z_x \beta^z_y \beta^o_y}}{2} \left[\frac{e^{i(\psi^o_y - \psi^z_y + \psi^z_x + 2\pi(2Q_x - Q_y))}}{1 - e^{2\pi i (Q_x - Qy)}} - \frac{e^{i(-\psi^o_y + \psi^z_y + \psi^z_x + 2\pi(2Q_x + Q_y))}}{1 - e^{2\pi i (Q_x + Qy)}} \right] \sum_s V^s_{1,0} \tag{16}$$

$$V_{0,0} = -b_3 j_x \sqrt{\beta^z_x \beta^z_y \beta^o_y} \left[\frac{e^{i(-\psi^o_y + \psi^z_y - \psi^z_x + 2\pi Q_y)}}{1 - e^{2\pi i Q_y}} \frac{e^{i(\psi^o_y - \psi^z_y - \psi^z_x - 2\pi Q_y)}}{1 - e^{-2\pi i Q_y}} \right] \sum_s V^s_{1,0}. \tag{17}$$

8 Analysis Including Octupoles and Sextupoles

The limited number of BPMs and the distributed nature of the sextupolar and octupolar fields around the SPS ring, results in a pattern of the modes $V_{2,0}$ and $V_{0,0}$ indistinguishable from the one produced by the crab-cavity. Therefore the only possible approach is to estimate and get rid of the octupoloes and sextupoles contributions relying solely on the knowledge of the SPS non-linear model. The study of the SPS non-linear optics carried out in 2017 [14] is used here as a reference. In addition to the chromatic sextupoles (for chromaticity correction), this model includes the field error of the 744 dipoles that is dominated by a non-negligible sextupolar distortion. Some octupolar field has also been measured but its exact origin is still debated. Two possible configurations for the residual octupolar field have been proposed and considered equally valid. The first configuration assumes a remanent octupolar field in the Landau octupoles, while the second one introduces the octupolar field as an error in the quadrupoles field. Both configurations have been tested.

To provide a rough idea of the importance of the contribution of octupoles and sextupoles to the analysis, the two families of multipoles are first analyzed individually. The contribution to the modes $V_{2,0}$ and $V_{0,0}$ are calculated separately for sextupoles and octupoles and fitted with the crab-cavity analytical model (Eq. (4) and (5)). The results of the fit (Fig. 14) show how normal octupoles and sextupoles have a dominant role in the analysis compared to the measured value of a_3 during the crab-cavity test and therefore should not be neglected. Finally we proceed to include the contribution of octupoles and sextupoles in the analysis. Starting from the SPS optics model and measured vertical closed orbit shift induced by the crab-cavity, the octupoles and sextupoles contributions are removed from the measured $V_{2,0}$ and $V_{0,0}$ before proceeding with the fit of the crab-cavity induced a_3. The results of the analysis are summarized in Table 3. As expected $a_3^{V_{2,0}}$ and $a_3^{V_{0,0}}$ show a strong dependency on the SPS non-linear model, and both models taken under consideration fail to provide a consistent and conclusive result. Between the two non-linear models the one that localize

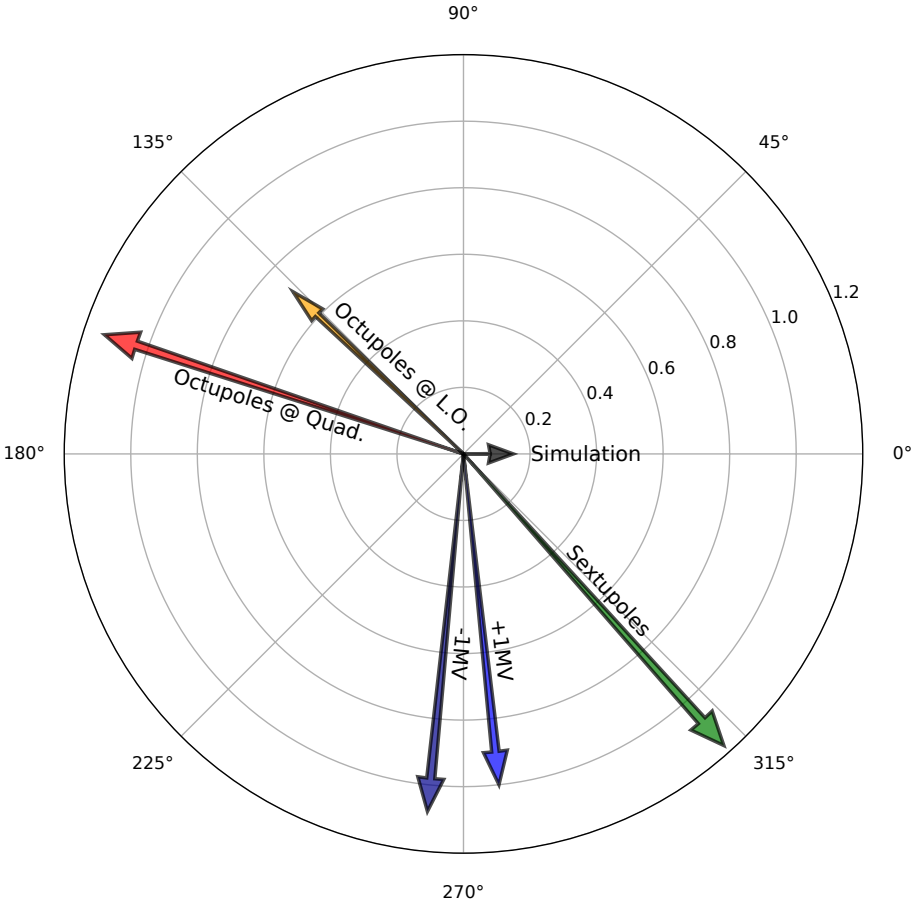

Figure 14: The value of a_3 inferred from the fit of the $V_{2,0}$ mode is shown as a complex vector. The a_3 derived from experimental data is consistent between the two acquisitions obtained with a crab-cavity voltage of $\pm 1\,\mathrm{MV}$ but exhibits a large phase. The a_3 derived from the two octupoles configurations shows a somehow similar result in phase and amplitude while the contribution from the normal sextupoles is diametrically opposed. For reference also the a_3 derived from RF simulations is shown.

the octupolar field at the quadrupoles seems more convincing, showing a smaller value of the complex part of $a_3^{V_{2,0}}$ (attested by the smaller value of the angle ψ). Finally, in the attempt to obtain a more precise estimate of $a_3^{V_{2,0}}$ the fit of the mode $V_{2,0}$ has been repeated a second time using both configurations of the octupoles model, but constraining again ψ to 0. This condition should provide a result in some extent immune to other sources driving the mode $V_{2,0}$ but likely with a different phase with respect to the crab-cavity. The results are collected in Table 4 while a plot of the fit for the configuration with octupolar fields at the quadrupoles is shown in Fig.15.

Table 3: Value of the skew-sextupolar integrated field obtained in every configuration under test with and without removing the contribution from normal sextupoles and octupoles. The two possible octupoles configuration from the SPS non-linear model have been taken into consideration.

Configuration	Δfield [MV]	ψ [deg]	$\lvert a_3^{V_{2,0}} \rvert$ [1/(m^2·MV)] [T/(m·MV)]	$a_3^{V_{0,0}}$ [1/(m^2·MV)] [T/(m·MV)]
No correction	0.762	-82.4±2.5	$2.046 \cdot 10^{-2} \pm 8.6 \cdot 10^{-4}$	$2.512 \cdot 10^{-2} \pm 4.0 \cdot 10^{-3}$
			$0.887 \pm 3.7 \cdot 10^{-2}$	$1.089 \pm 1.8 \cdot 10^{-1}$
Sext.+Oct. (Qaud.)	0.762	-40.7±2.5	$1.282 \cdot 10^{-2} \pm 8.2 \cdot 10^{-4}$	$3.438 \cdot 10^{-2} \pm 4.0 \cdot 10^{-3}$
			$0.556 \pm 3.6 \cdot 10^{-2}$	$1.490 \pm 1.7 \cdot 10^{-1}$
Sext.+Oct. (Landau)	0.762	-105.5±3.9	$1.214 \cdot 10^{-2} \pm 8.4 \cdot 10^{-4}$	$2.606 \cdot 10^{-2} \pm 4.0 \cdot 10^{-3}$
			$0.526 \pm 3.6 \cdot 10^{-2}$	$1.129 \pm 1.8 \cdot 10^{-1}$
No correction	-0.621	-84.2±2.2	$2.492 \cdot 10^{-2} \pm 9.9 \cdot 10^{-4}$	$-2.039 \cdot 10^{-2} \pm 5.5 \cdot 10^{-3}$
			$1.080 \pm 4.3 \cdot 10^{-2}$	$-0.884 \pm 2.4 \cdot 10^{-3}$
Sext.+Oct. (Quad.)	-0.621	-53.6±3.6	$1.611 \cdot 10^{-2} \pm 9.9 \cdot 10^{-4}$	$-1.179 \cdot 10^{-2} \pm 5.4 \cdot 10^{-3}$
			$0.698 \pm 4.3 \cdot 10^{-2}$	$-0.511 \pm 2.4 \cdot 10^{-3}$
Sext.+Oct. (Landau)	-0.621	-101.9±3.2	$1.650 \cdot 10^{-2} \pm 9.6 \cdot 10^{-4}$	$-1.887 \cdot 10^{-2} \pm 5.5 \cdot 10^{-3}$
			$0.715 \pm 4.2 \cdot 10^{-2}$	$-0.818 \pm 2.4 \cdot 10^{-3}$

Table 4: Values of the skew-sextupolar integrated field derived from the fit of $V_{2,0}$ only, after having removed the contribution from normal sextupoles and octupoles. The two possible octupoles configuration from the SPS non-linear model have been taken into consideration. In order to get an estimate of a_3 as immune as possible from other sources driving the mode $V_{2,0}$ the phase ψ has been constrained to 0.

Configuration	Measured Δfield [MV]	$a_3^{V_{2,0}}$ [1/(m^2·MV)]	$a_3^{V_{2,0}}$ [T/(m·MV)]
Sext. + Oct. (Landau)	0.762	$-2.680 \cdot 10^{-3} \pm 1.2 \cdot 10^{-3}$	$-0.1161 \pm 5.1 \cdot 10^{-2}$
Sext. + Oct. (Landau)	-0.621	$9.953 \cdot 10^{-3} \pm 1.3 \cdot 10^{-3}$	$0.431 \pm 5.8 \cdot 10^{-2}$
Sext. + Oct. (Quad.)	0.762	$1.012 \cdot 10^{-2} \pm 1.0 \cdot 10^{-3}$	$0.438 \pm 4.5 \cdot 10^{-2}$
Sext. + Oct. (Quad.)	-0.621	$-2.957 \cdot 10^{-3} \pm 1.5 \cdot 10^{-3}$	$-0.1282 \pm 6.4 \cdot 10^{-2}$

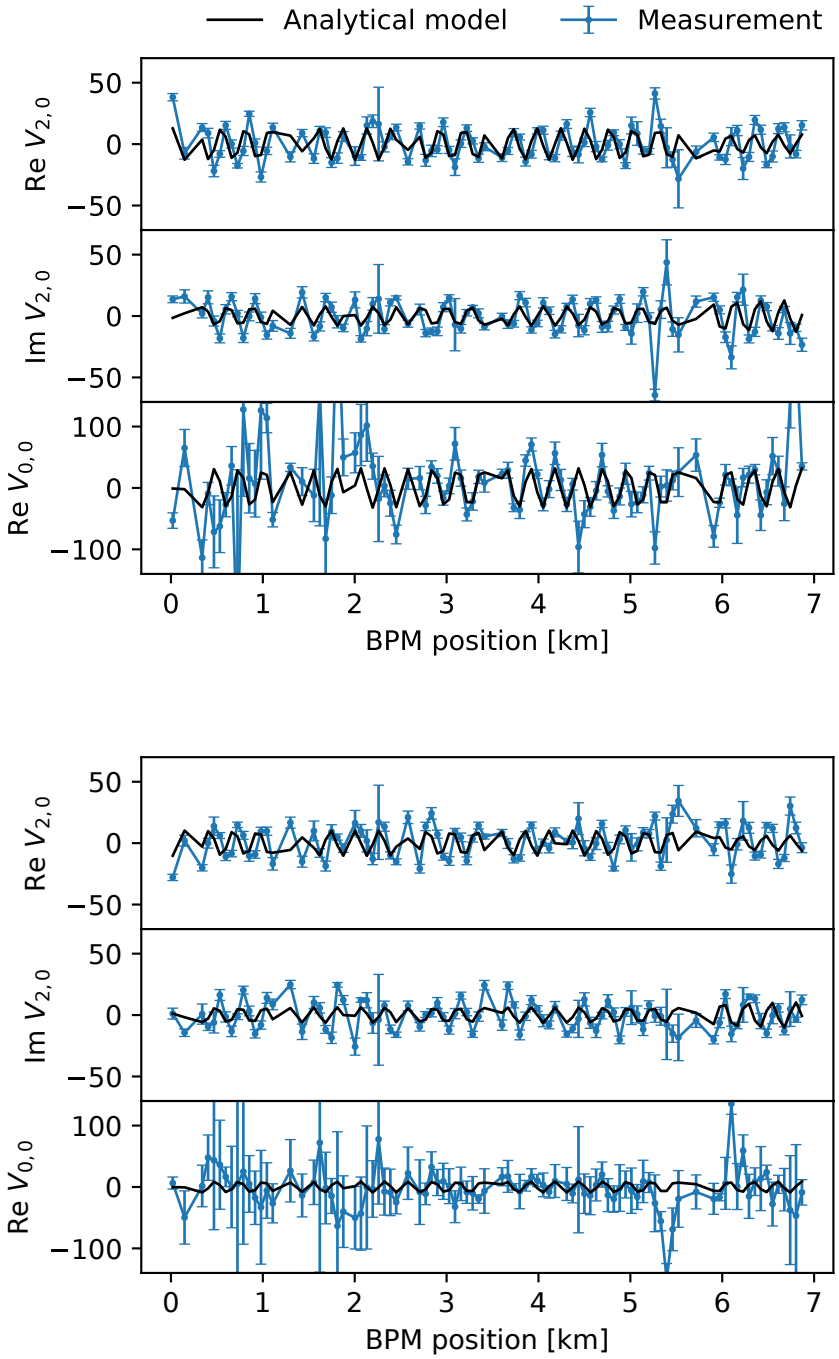

Figure 15: Variation (blue) of the real and imaginary part of the $V_{2,0}$ and $V_{0,0}$ modes induced by switching on the crab-cavity field from 100 kV to ∼1 MV (top) and from 100 kV to ∼−1 MV (bottom). No additional imaginary part was allowed to a_3 during the fit, but the contribution to $V_{2,0}$ and $V_{0,0}$ due to normal sextupoles and octupoles have been removed from the experimental data before running the fit. The octupoles model used in this case is the one with octupolar errors at the quadrupoles, a similar result is obtained for the other configuration (remanent field in the octupoles).

9 Conclusions

An attempt to estimate the value of the skew-sextupolar component a_3 of the LHC crab-cavity has been carried out, relying on the spectral analysis of the turn-by-turn non-linear betatron motion. A first test was carried out using a static skew-sextupolar field, showing positive results and proving the validity of the experimental technique and analysis tools. A short time span was assigned for crab cavity tests in October 2018 during which the measurement was carried out. The quality of the measured data appeared to be comparable to what was observed in the previous test, despite the reduced statistics due to the time constraints. It was found how the small signal produced by the skew-sextupolar field of the Crab-Cavity was easily polluted by second order effects from normal octupoles and sextupoles triggered by the substantial vertical orbit induced by the crab-cavity itself. Because of the impossibility to carry out more measurements an attempt to estimate and remove the contributions of sextupoles and octupoles relying on the current knowledge of the SPS non-linear model was undertaken. The very small entity of the crab-cavity signal compared to the already existing non linearity in the SPS optics made the task particularly challenging. The uncertainties in the SPS non-linear model did not allow to derive a completely self consistent result, and some contribution from the optics non-linearities are to be expected. Therefore the fit results are to be considered as an overestimation of the real crab-cavity skew-sextupolar field. Following this assumption, by relying on the observation of the mode $V_{2,0}$ that happen to be in a certain measure more immune to the contributions of spurious effects of the SPS non-linear optics, it is possible to restrict the a_3 value to the range $-0.13\,\mathrm{T}/(\mathrm{m}\cdot\mathrm{MV})$ to $0.43\,\mathrm{T}/(\mathrm{m}\cdot\mathrm{MV})$, to be compared with the value of $0.15\,\mathrm{T}/(\mathrm{m}\cdot\mathrm{MV})$ provided by RF simulations.

10 Acknowledgments

We are grateful to Y. Papaphilippou, G. Arduini and R. Tomàs for proofreading the original manuscript, and to R. Tomàs also for stressing the importance of second order effects into the analysis and the many fruitful discussions. We would like to thank James Alexander Mitchell and Emilia Cruz Alaniz for discussing the crab-cavity RF measurements, and Riccardo De Maria for helping with the interpretation of crab-cavity RF simulations results. We would like to thank also the SPS operation group for assisting with the machine set-up.

Appendix

A Forced betatron motion

The transverse betatron motion of a particle under the influence of an external harmonic driving force is derived here following a procedure similar to what is used in [15, 16]. Normal form analysis is also another viable and largely used approach [17, 18, 19, 20]. On the other hand the complexity of the required mathematical formalism is likely to hide the otherwise simple physical mechanisms that leads to the dynamics under study. Being not strictly

required in this specific case, we prefer to avoid normal form analysis in favor of a more agile approach. The driving force is localized in a thin insert that at turn n results in a transverse kick on the beam:

$$\delta p(n) = A^d \cdot \sin(2\pi Q_d n + \psi_0), \tag{18}$$

where Q_d is the driving force frequency, A^d is an amplitude parameter and the phase ψ_0 takes into account for the initial phase of the driving force. Thus the transverse action change $\delta j(n)$ associated with the kick $\delta p(n)$ is:

$$\delta j(n) = \frac{\delta p^2(n) \cdot \beta^d}{2}, \tag{19}$$

with β^d the betatron amplitude at the driving force location. The change in action $\delta j(n)$ at turn n is associated with a free betatron motion that at turn t has the amplitude:

$$x_n(t) = \sqrt{2\delta j(n)\beta^o} \cdot \sin(2\pi Q(t-n) + \psi^o - \psi^d), \tag{20}$$

where Q is the natural betatron tune, β^o is the betatron amplitude of the observation point (e.g. BPM) and $\psi^o - \psi^d$ is the phase advance between the observation point and the driving force location. The overall betatron motion observed at turn t induced turn after turn by the repeated action of the driving force is obtained by summing Eq. (20) over n:

$$x(t) = \sum_{n=0}^{n=t} \sqrt{2\delta j(n)\beta^o} \cdot \sin(2\pi Q(t-n) + \psi^o - \psi^d), \tag{21}$$

where the sum starts from turn the betatron motion is excited by firing the tune kicker, that is arbitrarily assumed to happen at turn $n = 0$. It is important to remember that in every case studied here the driving force is the actual result of the interplay of a non-linear magnetic field and the linear betatron motion rather than a an external driving force. This condition ensures that the driving force is zero before turn $n = 0$, when the kicker is fired. Combining Eqs. (18), (19) and (21) yields:

$$x(t) = \sum_{n=0}^{n=t} A^d \sqrt{\beta^d \beta^o} \cdot \sin(2\pi Q_d n + \psi_0) \dot{\sin}(2\pi Q(t-n) + \psi^o - \psi^d), \tag{22}$$

which after some manipulation can be written as:

$$x(t) = \Re \sum_{n=0}^{n=t} \frac{A^d}{2} \sqrt{\beta^d \beta^o} \left[e^{2\pi i (Q_d + Q) n} \cdot e^{i(\psi_0 - 2\pi Q t - \psi^o + \psi^d)} - e^{2\pi i (Q_d - Q) n} \cdot e^{i(\psi_0 + 2\pi Q t + \psi^o - \psi^d)} \right]. \tag{23}$$

The sum is written in closed form with the help of the geometric series property:

$$\sum_{n=0}^{n=t} r^n = \frac{1 - r^{t+1}}{1 - r}, \tag{24}$$

providing:

$$x(t) = \Re \frac{A^d}{2} \sqrt{\beta^d \beta^o} \left[\frac{e^{i(\psi_0 - 2\pi Q t - \psi^o + \psi^d)} - e^{i(2\pi(Q_d t + Q_d + Q) + \psi_0 - \psi^o + \psi^d)}}{1 - e^{2\pi i (Q_d + Q)}} + \right. \\ \left. - \frac{e^{i(\psi_0 + 2\pi Q t + \psi^o - \psi^d)} - e^{i(2\pi(Q_d t + Q_d - Q) + \psi_0 + \psi^o - \psi^d)}}{1 - e^{2\pi i (Q_d - Q)}} \right]. \tag{25}$$

Interestingly the previous expression always consists of the sum of two terms, one with the same frequency of the driving force Q_d, and a second one with frequency Q. This last term results from the transient nature of the excitation provided by the tune kicker, and instead it disappears if gradually exciting (adiabatically ramping) the linear betatron motion (in the limit of an infinite ramp this condition is equivalent to extend the lower bound of the sum in Eq. (21) from 0 to $-\infty$). From an experimental point of view this last mode, having the same frequency of the natural tune is virtually impossible to distinguish from the free betatron motion and therefore is usually discarded. Finally after removing this superfluous term, the driven betatron motion reduces to:

$$x(t) \simeq \Re \left[H \cdot e^{2\pi i Q_d t} \right], \tag{26}$$

with:

$$H = \frac{A^d}{2} \sqrt{\beta^d \beta^o} \left[\frac{e^{i(2\pi(Q_d - Q) + \psi_0 + \psi^o - \psi^d)}}{1 - e^{2\pi i (Q_d - Q)}} - \frac{e^{i(2\pi(Q_d + Q) + \psi_0 - \psi^o + \psi^d)}}{1 - e^{2\pi i (Q_d + Q)}} \right]. \tag{27}$$

References

[1] G. Apollinari, I. Béjar Alonso, O. Brüning, P. Fessia, M. Lamont, L. Rossi and L. Tavian, CERN Yellow Rep. Monogr. **4**, 1 (2017). doi:10.23731/CYRM-2017-004

[2] L. Rossi, Progress with the High Luminosity LHC Programme at CERN, presented at the 10th Int. Particle Accelerator Conf. (IPAC19), Melbourne, Australia, May 2019, this conference.

[3] Y. P. Sun, R. Assmann, J. Barranco, R. Tomas, T. Weiler, F. Zimmermann, R. Calaga and A. Morita, "Beam dynamics aspects of crab cavities in the CERN Large Hadron Collider" Phys. Rev. ST Accel. Beams **12**, 101002 (2009). doi:10.1103/PhysRevSTAB.12.101002

[4] J. Barranco García, R. De Maria, A. Grudiev, R. Tomás García, R. B. Appleby and D. R. Brett, "Long term dynamics of the high luminosity Large Hadron Collider with crab cavities" Phys. Rev. Accel. Beams **19**, no. 10, 101003 (2016). doi:10.1103/PhysRevAccelBeams.19.101003

[5] James Alexander Mitchell, "Higher Order Modes and Dampers for the LHC Double Quarter Wave Crab Cavity" Ph.D. dissertation, Un. of Lancaster, https://doi.org/10.17635/lancaster/thesis/743

[6] L.R. Carver *et al.*, "First proton beam dynamics results with crab cavities", in Proc. 10th Int. Particle Accelerator Conf. (IPAC19), Melbourne, Australia, May 2019, paper MOPGW094, this conference.

[7] C. Boccard *et al.*, CERN-SL-99-048-BI, CERN-SL-99-48-BI.

[8] J. Laskar, C. Froeschlé and A. Celletti, "The measure of chaos by the numerical analysis of the fundamental frequencies. application to the standard mapping", Physica D: Nonlinear Phenomena, 56(2):253 269, 1992.

[9] J. Laskar, Conf. Proc. C **030512**, 378 (2003).

[10] Y. Papaphilippou, Chaos **24**, 024412 (2014) doi:10.1063/1.4884495 [arXiv:1406.1545 [nlin.CD]].

[11] R. E. Meller, A. W. Chao, J. M. Peterson, S. G. Peggs and M. Furman, "Decoherence of Kicked Beams," SSC-N-360.

[12] R. Tomàs, "Direct measurement of resonance driving terms in the SPS of CERN using beam position monitors," Ph.D. thesis, University of Valencia, Spain, 2003 [Report No. CERN-THESIS-2003-010].

[13] A. Alekou *et al.*, "Deliverable 2.10: Summary of the observations in the SPS and update of the estimates for HL-LHC," CERN-ACC-2020-0002.

[14] M. Carlà *et al.*, "Assesment of the SPS non-linear model from beam based measurements," in preparation.

[15] R. Miyamoto, "Diagnostics of the Fermilab Tevatron Using an AC Dipole" Ph.D. thesis, The University of Texas at Austin, 2008

[16] J. Bengtsson, "Non-linear transverse dynamics for storage rings with applications to the low-energy antiproton ring (LEAR) at CERN" Presented on 1 Aug 1988, 10.5170/CERN-1988-005

[17] A. Bazzani *et al.*, "Normal forms for Hamiltonian maps and non linear effects in aparticle accelerator," Nuovo Cim. B102, 51-80 (1988).

[18] A. Bazzani, E.Todesco, G.Turchetti and G. Servizi, "A normal form approach to the theory of nonlinear betatronic motion," CERN94-02 (1994)

[19] M. Berz, E. Forest and J. Irwin, "Normal form methods for complicated periodic systems: a complete solution using differential algebra and lie operators," Particle Accelerators, Vol 24, 91-107 (1989)

[20] R. Bartolini and F. Schmidt "Normal form via tracking or beam data" Particle Accelerators, Vol. 59, pp. 93-106 (1997)